Journal of Computational Physics **159,** 38–57 (2000)
doi:10.1006/jcph.2000.6419, available online at http://www.idealibrary.com on IDEAL®

# Simultaneously Resolved Bifurcation Diagrams: A Novel Global Approach Applied to Liquid Figures of Equilibrium

Gábor Domokos,* Imre Szeberényi,† and Paul H. Steen‡

**Department of Strength of Materials and †Department of Control Engineering and Information Technology, Technical University of Budapest, H-1521 Budapest, Hungary; and ‡Department of Chemical Engineering and Center for Applied Mathematics, Cornell University, Ithaca, New York 14853*
E-mail: *domokos@iit.bme.hu, †szebi@iit.bme.hu, and ‡phs7@cornell.edu

Received June 10, 1999; revised November 24, 1999

A new approach to the computation of bifurcation diagrams is illustrated on axisymmetric equilibria of liquid droplets and bridges. The new technique has an architecture that solves boundary-value problems in parallel and delivers a global bifurcation diagram, capturing isolated branches. In contrast, conventional techniques deliver solutions in sequence using local path continuation. A suitable mathematical formulation for the classical problem of predicting shapes of droplet and bridge equilibria is introduced and it its shown how the new technique yields global diagrams. Properties of these diagrams allow families of equilibria to be organized in a way that reveals common structures. © 2000 Academic Press

*Key Words:* bifurcation; ODE; BVP; liquid bridges; liquid drops.

## 1. INTRODUCTION

In this paper we will illustrate a new computation technique for the efficient utilization of parallel resources, using the example of liquid figures of equilibrium. We will show that the new computational approach not only provides a complete global picture of bifurcation problems but also helps to relate physical problems with different parameters.

The computational approach, introduced by [10, 11, 14], is based on some simple ideas from the theory of ordinary differential equations (ODEs), combined with the piecewise linear (PL) algorithm [1], and will be referred to henceforth as the parallel simplex algorithm (PSA). In contrast to path-continuation techniques, which solve for equilibria in sequence in tracing a branch, the PSA simultaneously resolves *all* equilibria lying on *all* branches (in a given domain). Although simple shooting remains at the core of the PSA, the combination of shooting with the PL algorithm offers a good alternative to traditional methods if the

0021-9991/00 $35.00

underlying ODE is not very sensitive to the perturbation of initial conditions. In this paper we describe the application of the PSA to such a problem and refer to other applications in mechanics where it could be used successfully.

Instead of giving a general description (which is provided by the above-cited papers), we will proceed in Section 2 by formulating the problem of determining the shape of droplets and bridges as an initial-value problem (IVP). In Section 3 we will apply the PSA to bridges and droplets and describe the implementation. Section 4 is devoted to the description and discussion of results of computations.

The PSA can be directly applied to two-point boundary-value problems (BVPs) associated with ODEs. Assuming that the latter is of even order (which is most often the case in mechanics), it is equivalent to $\dot{x}(t) = f(x(t), \lambda)$, $x \in \Re^{2n}$, $\lambda \in \Re$, $t \in [0, 1]$. Let us regroup the equations so that the initial ($t = 0$) conditions apply to the first $n$ components ($x_i(0) = a_i$, $i = 1, 2, \ldots, n$) and far-end ($t = 1$) conditions apply to the those with indices $\nu_i$ ($x_{\nu_i}(1) = b_i$, $i = 1, 2, \ldots, n$), where $a_i, b_i$ are given scalars. We denote the remaining initial conditions or *variables* by $v_{i-n} = x_i(0)$, $i = n+1, n+2, \ldots, 2n$. The $(n+1)$-dimensional space spanned by the variables and the parameter $\lambda$ is called the global representation space (GRS). Using any convergent forward integrator for the IVP, we can compute the final values $x_{\nu_i}(1)$, ($i = 1, 2, \ldots, n$) as *functions* of $v_i$ and $\lambda$: $x_{\nu_i} = g_i(v_1, v_2, \ldots, v_n, \lambda)$ and then solve the algebraic system

$$g_i(v_j, \lambda) - b_i = 0; \qquad i, j = 1, 2, \ldots, n, \ \ v_j \in \left[v_j^0, v_j^1\right], \quad \lambda \in [\lambda^0, \lambda^1] \tag{1}$$

by the PL algorithm [1] in the prescribed $(n+1)$-dimensional domain of the GRS (defined by the constants with superscript in (1)). Geometrically, (1) describes the intersection of $n$ hyper-surfaces in the $(n+1)$-dimensional space, yielding typically (locally) 1-dimensional solution sets, thus branches. These branches will appear as polygons, due to the piecewise linear approximation. (We remark that the variables can have a far more general interpretation in the PSA; however, the above version is sufficient to introduce the most important concepts.)

Although the key ideas of the PSA are rather easily described, this approach is not very widespread in the computational community. It requires in many cases massive hardware capabilities, but so do path continuation methods. However, one key difference between the two approaches is historic. Present, very efficient, and sophisticated path continuation codes [8, 9, 30] evolved on the basis of earlier, less refined ones which, in turn, were the direct successors of hand-computed methods. There is no such “baggage” associated with the PSA, since a small-scale version would be not only cumbersome but of little use. The other reason for the lack of tradition is the recent appearance of parallel computers and the possibility of parallel computation on distributed networks. Parallel computation is at the core of the PSA, although for test purposes, it can be run on a single node. We remark that there exist other algorithms that combine search with path continuation [17]; however, the search is restricted to solution points rather than branches.

Application of the method can be visualized without technical details. System (1) can be resolved simultaneously in any subdomain of the GRS. “Simultaneous resolution” stands in relation to “continuation” as photographic imaging stands to freehand sketching. The pixels of a film negative are developed simultaneously (in parallel) in a chemical bath, whereas the hand sketch requires a sequence of strokes with each point in a stroke laid down sequentially. Developing this analogy further, we note that bifurcation diagrams obtained by continuation are like hand sketches where the pencil cannot lift whereas simultaneous resolution can deliver families of equilibria that are unconnected (e.g., isolas). These features make the PSA an optimal candidate for the relatively fast, global understanding of low-dimensional bifurcation problems [10, 11, 14, 19]. Limitation of the method to low-dimensional problems is due to computational demand and is discussed in the concluding section.

Liquid equilibria problems are low dimensional. The GRS is only 2-dimensional for a wide range of physical situations, as seen in Sections 2 and 3. Scientific interest in figures of equilibrium can be traced back to the time of Plateau [28]. Mathematicians have been stimulated by the minimal surface problem and by capillary surface interfaces [13, 37, 39] Physical chemists have made early computations of shapes. Motivation has ranged from improving measurement devices where a meniscus is involved [3] to measuring surface tension using droplet and bubble methods [2, 4]. Recent interest from the engineering community has focussed on materials [5, 7] and microgravity applications [26, 27]. The common feature here is that liquid shapes are dominated by surface tension (large capillary length). In these papers, by concentrating on different physical aspects (such as effects of gravity, asymmetric boundary conditions, etc.) unifying features easily recognized in the setting of the GRS have been obscurred. Our present goal is to show that the PSA not only can utilize parallel computing resources very efficiently in order to solve such problems but also can help to understand the relationship among them by putting bifurcation diagrams in a common geometrical setting.

## 2. FORMULATION OF THE GOVERNING EQUATIONS

### 2.1. *Liquid Shapes as IVPs: A Dynamical Systems Approach*

Static shapes of surfaces that contain a liquid are governed by the normal stress balance across the surface, called the Young–Laplace equation. This requires the pressure $p$ in the liquid to be proportional to the surface tension $\sigma$ and to the sum of the principal curvatures, $\kappa_1 + \kappa_2$ (cf. [23, 27] or [40]),

$$p = \sigma(\kappa_1 + \kappa_2). \tag{2}$$

A pressure within the bridge that is below that of the surroundings (vacuum) is negative. For surfaces of revolution of a $rz$ plane curve (cf. Fig. 1a), the principal curvatures can be expressed in terms of $\alpha$, the (counterclockwise positive) angle with respect to the $r$ axis (i.e., $\tan\alpha \equiv \dot{z}/\dot{r}$),

$$\begin{aligned} \kappa_1 &= \sin(\alpha)/r, \\ \kappa_2 &= \dot{\alpha}. \end{aligned} \tag{3}$$

Arclength $s$ is the independent variable ($\dot{} \equiv d/ds$) in this “tangent-angle” formulation, a common one for computing capillary equilibria [2]. In terms of $\alpha$, the Young–Laplace equation (2) takes the form of the ODE system

$$\begin{aligned} \dot{\alpha} &= p + Bz - \sin(\alpha)/r \\ \dot{r} &= \cos(\alpha) \\ \dot{z} &= \sin(\alpha), \end{aligned} \tag{4}$$

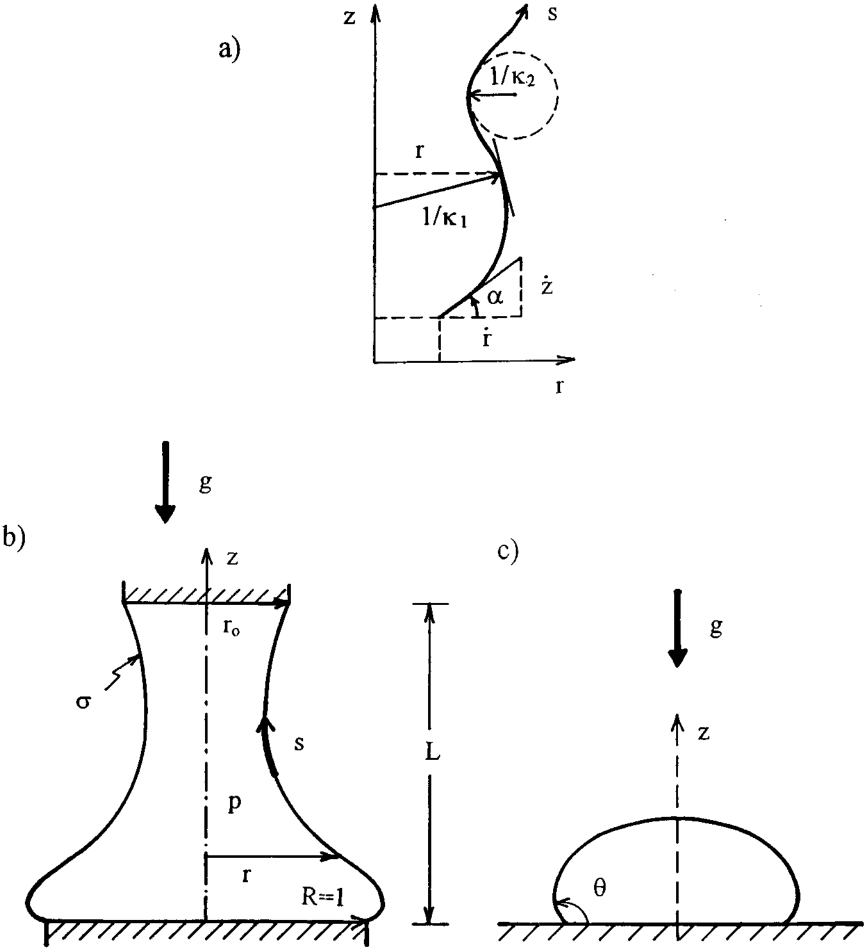

**FIG. 1.** Definition sketches for axisymmetric figures of equilibrium: (a) space-curve geometry or “kinematics” for the IVP; (b) liquid bridge BVP; (c) liquid droplet BVP.

where reduced quantities have been used and the effect of gravity $g$ acting on the liquid in the $z$ direction has been included. In particular, dimensional variables, denoted with overbars, are related to the reduced variables by

$$r \equiv \bar{r}/R, \qquad z \equiv \bar{z}/R, \qquad s \equiv \bar{s}/R, \qquad \kappa \equiv \bar{\kappa}R, \qquad p \equiv \bar{p}R/\sigma.$$

The Bond number $B \equiv \rho g R^2/\sigma$ depends on the liquid density $\rho$ (relative to surroundings) and a contact radius $R$.

The local equations (4) can be integrated in $z$ to obtain the total reaction force $F$ ($F \equiv \bar{F}/(\pi R\sigma)$) exerted by any segment of surface-bounded liquid of length $z$,

$$F = 2r\sin\alpha - pr^2 + B\{V(z) - zr^2\}, \tag{5}$$

where $V(z) \equiv \int_0^z r^2\,dz$ represents the scaled volume of the segment ($V \equiv \bar{V}/R^3$). Note that $F$ is a constant in the integral constraint (5).

In the special no-gravity case ($B = 0$), (4) reduces to

$$\begin{aligned} \dot{\alpha} &= p - \sin(\alpha)/r \\ \dot{r} &= \cos(\alpha). \end{aligned} \tag{6}$$

The third equation decouples from the system and can be integrated separately once $\alpha(s)$ is known. The solution structure and the dynamics are completely determined by (6), which turns out to be completely integrable [18] with first integral

$$F = 2r \sin\alpha - pr^2. \tag{7}$$

Equation (7) is recognized as the $B = 0$ subcase of the force balance (5).

Individual trajectories appear as *level sets* of $F$ in the $\alpha r$ phase plane. In fact, the topology of the phase space is that of a *cylinder* since $\alpha$ is $2\pi$-periodic, so we will consider only $\alpha \in [-\pi, \pi]$. The fixed points of the flow are associated with extrema of $F$ and can be found by letting the derivatives vanish,

$$\dot{\alpha} = \dot{r} = 0, \tag{8}$$

leading to

$$\begin{aligned} (\alpha, r) &= \left(\frac{\pi}{2}, \frac{1}{p}\right) \\ (\alpha, r) &= \left(-\frac{\pi}{2}, -\frac{1}{p}\right). \end{aligned} \tag{9}$$

Here, even though the formulation derives from a cylindrical coordinate system ($r \geq 0$), the interpretation of system (4) as an IVP clearly permits negative $r$. The fixed points appear in the $rz$ physical space as straight vertical lines at $r = \pm 1/p$. These are right-circular cylinders in 3D space. We can identify other special solutions by requiring the curvature $\dot{\alpha}$ to be constant, leading to

$$r = \frac{2\sin(\alpha)}{p}. \tag{10}$$

These solutions appear in the $rz$ space as circles with center on the $z$-axis and radius equal to $2/p$. The line $r = 0$ in the phase space is singular since $r = 0$ is only admitted at $\alpha = 0$. At the intersection point we have $\dot{\alpha} = p/2$. The special trajectory (10) and the singular solution separate the phase space into an open domain and two closed domains, the latter one containing the fixed points. The eigenvalues of the linearized map prove to be $\lambda_{1,2} = \pm i/p$, purely imaginary, so the fixed points are elliptic and there are closed orbits encircling them, remaining in the closed domains.

Based on the above information we can draw the global phase portrait of the system (6), revealing four types of trajectories (cf. Fig. 2a). Interpretations of these trajectories in the phase plane $\alpha r$, the physical plane $rz$ and as surfaces of revolution are listed in Table I. We note that these results are classical. All the trajectories can be expressed in closed from in terms of elliptic integrals of the first and second kind [15, 20].

The case $p = 0$ will be of special interest. In this case, since fixed points **A** escape to infinity, the **B**, **C**, and **D**-type orbits become similar and only one kind of orbit remains

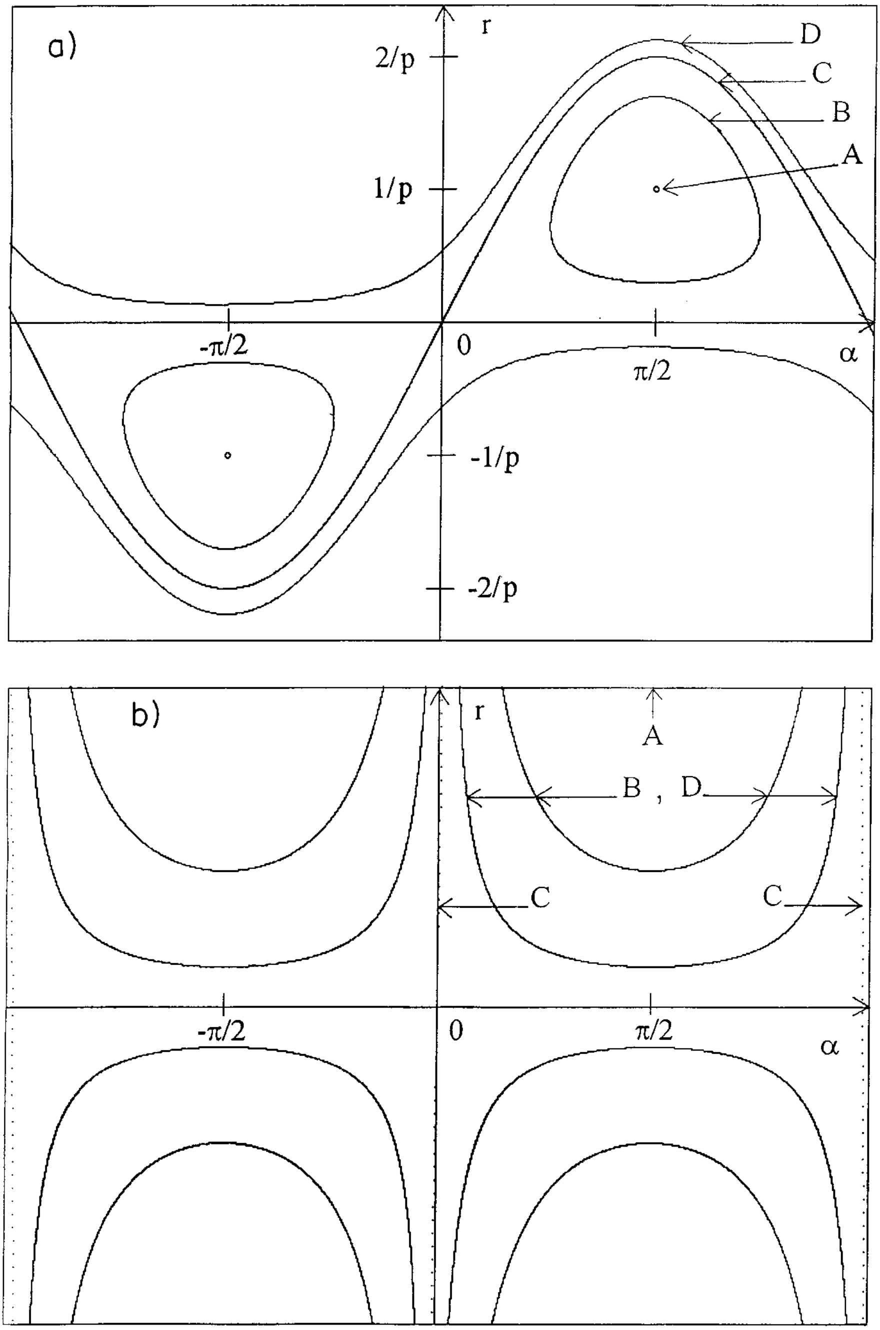

**FIG. 2.** Global phase portrait for $B = 0$: (a) typical case with $p > 0$; (b) degenerate case with $p = 0$.

(Fig. 2b). In the $rz$ plane, this trajectory represents a catenary. As a surface of revolution, it is known as a catenoid. This result is consistent with a classical theorem of differential geometry that the only surface of revolution that is a minimal surface (vanishing mean curvature) is the catenoid [21]. Based on the classification for the IVP orbits we now proceed to explore the global bifurcation diagram for the BVP.

**TABLE I**
**Different Types of Solutions**

| Type | $\alpha r$ plane | $rz$ plane | 3D surface |
|---|---|---|---|
| A | Fixed points | Straight lines | Cylinder |
| B | Closed orbits | Oscillations | Unduloid |
| C | Separatrix | Circle | Sphere |
| D | Open, oscillating orbits | Looping | Nodoid |

### 2.2. *Liquid Equilibria as BVPs: Implementing the PSA*

A variety of physical problems (BVP) associated with the ODE (4) have been studied. Boundary conditions considered for liquid bridge equilibria (6) may be either pinned contact line (Fig. 1b with $r_0 = 1$)

$$r(0) = r|_{z=L} = 1, \tag{11}$$

or fixed contact angle $\theta$ [22, 37],

$$\alpha(0) = \pi - \theta; \qquad \alpha|_{z=L} = \theta, \tag{12}$$

where $z$ is defined by the third equation of (4) with corresponding boundary condition

$$z(0) = 0. \tag{13}$$

Droplets with fixed contact angle (Fig. 1c) or pinned contact line may also be considered [39]. Substrate geometry and liquid/substrate chemistry determines which is appropriate in any physical situation. Single droplet equilibria can be recovered as a special case of the liquid bridge equilibria. Alternatively, the droplet problem can be formulated as a BVP on its own with a different GRS. This example will serve below to illustrate how different GRSs associated with the same physical problem deliver equivalent bifurcation diagrams. The computational aspects of the PSA are most clearly illustrated on weightless equlibria (6).

Consider the pinned contact line bridge with equal end disks ($r_0 = 1$). In order to apply the PSA to this BVP, we have to establish the global coordinates spanning the GRS. As described in the Introduction, these coordinates (variables) consist of unspecified initial values and parameters. In our case, the only unspecified initial value is $\alpha(0)$, which, with the parameter $p$, spans a 2-dimensional GRS. By using the coordinates $(\alpha(0), p)$ the physical $rz$ shape can be uniquely reconstructed by forward integration of (6) and the third equation of (4). Adopting the general notation of the Introduction, we have $n = 1$; $x_1 \equiv r$; $x_2 \equiv \alpha$, $a_1 = 1$, $\nu_1 = 2$, $v_1 \equiv \alpha(0)$, $\lambda \equiv p$.

Note that the far-end condition in (11) is not expressed for fixed value of arclength but as an integral constraint. This can lead to nonuniqueness. Indeed, the function $f(\alpha_0, p) \equiv \int_0^s \sin(\alpha) - L = z - L$ might have *several* zeroes as we integrate forward and the far-end condition of (11) does not distinguish between them. By labeling the subsequent values of the arclength corresponding to $f = 0$ in increasing order as $s_1, s_2, \ldots$, we can also label BVP solutions in a similar manner, and the BVP solution corresponding to $s_k$ will be called a *level k* solution, some examples of which are given in Fig. 3a. Each solution level is generated geometrically by the intersection of the 2D GRS with a piecewise continuous

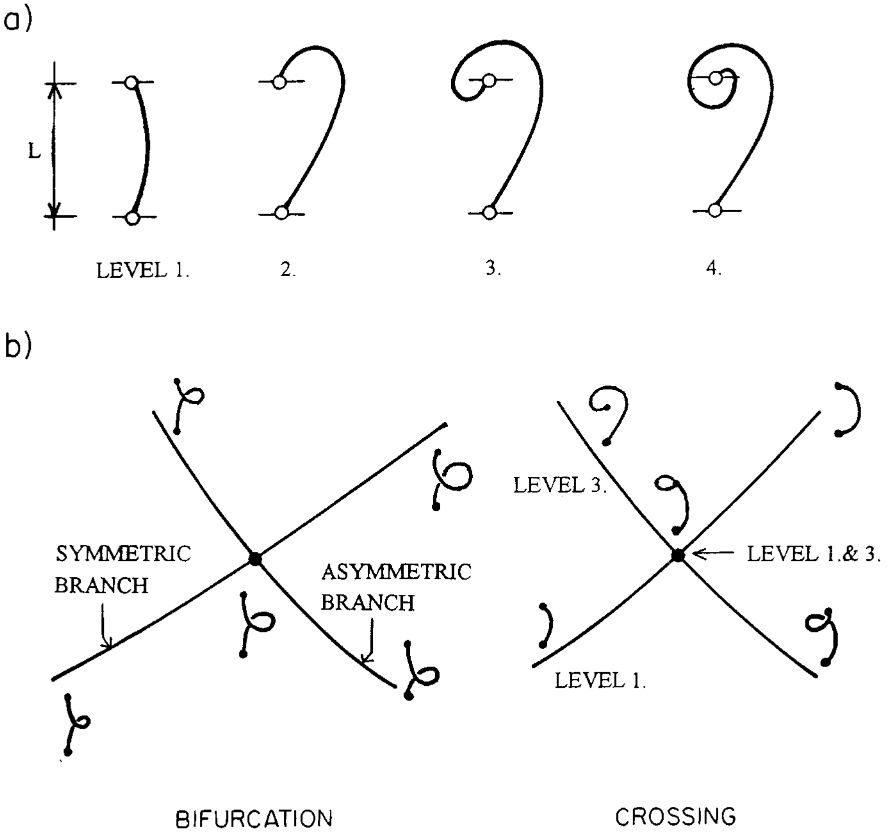

**FIG. 3.** Bifurcations and crossings: (a) individual solutions belonging to different levels; (b) intersecting branches on identical and different levels (bifurcations and crossings, respectively).

(and smooth) surface; different levels belong to different surfaces. This implies that, in order to reconstruct a BVP solution from its global coordinates, the integer $k$ is needed as well.

Projections of multiple solution levels onto the bifurcation diagram gives rise to two kinds of intersections of families. Bifurcations occur among solutions of the same level while “crossings” occur if branches belong to different levels. These different intersections respond differently to perturbations. Bifurcations “break” to become “imperfect” while crossings persist under perturbation. Bifurcations (generic) and crossings are schematically illustrated in Fig. 3b. For pinned liquid bridge equilibria between equal disks, for example, the bifurcations occur at $\alpha = \pm\pi/2$, as is well known (e.g., [25]) and as illustrated in Fig. 5.

Before the computations are described we mention another interesting qualitative feature of the bifurcation diagram. As we have seen in the preceding subsection, the IVP’s phase space is divided by a separatrix (C-type solution), corresponding to circular shapes. Quite surprisingly, an exact “image” of this separatrix appears on the BVP’s bifurcation diagram. In the case of the IVP, for *any* trajectory $(\alpha(s), r(s))$ it can be uniquely determined whether it is inside or outside the separatrix based on the coordinates of *any* single point on the trajectory. In the case of BVP solutions this point can be conveniently selected as $(\alpha(0), r(0)) = (\alpha(0), 1)$. As a consequence, the curve

$$p = 2\sin(\alpha(0)) \tag{14}$$

will separate BVP solutions in the GRS $(\alpha(0), p)$. *Below* the locus of (14) we have B-type solutions (unduloids), while *above* (14) we have D-type solutions (nodoids). Intersections with (14) correspond to C-type solutions (spheres). Refer to Table I.

The BVP separatrix (14) actually represents the solution branch of a *different* BVP belonging to the same IVP. The boundary conditions for this problem are

$$r(0) = 1, \qquad r|_{z=0} = -1 \tag{15}$$

and define single droplets (or bubbles) connected to a single disk instead of liquid bridges. Although the boundary conditions (11) and (15) appear to be different, they are closely related from the point of view of the PSA. Both BVPs have the same phase space and GRS. The solutions corresponding to (15) can be easily identified in the phase space, since we know that the only trajectory crossing the $r = 0$ singular line is the separatrix. Consequently, (15) can have only solutions that are segments of the separatrix, and thus they are the C-type circular solutions (spheres).

We have just seen how different physical problems have different BVPs corresponding to the same IVP. It is also possible to have different GRSs for the same physical problem. We illustrate with the droplet problem (ODE (6)). As an alternative to (15), the droplet BVP may be defined by conditions applied at the axis of symmetry at some (unknown) height $z(0)$,

$$\alpha(0) = r(0) = 0, \qquad r|_{z=0} = 1. \tag{16}$$

Here, the GRS is $(z(0), p)$ and the end condition takes the form of a constraint $g(z(0), p) - b \equiv r|_{z=0} - 1 = 0$ whose solution is the bifurcation curve. As indicated above, the IVP can be solved in closed form for equilibria that are pieces of spheres. The bifurcation equation, in this case, is explicit,

$$g(z(0), p) - b = (z(0) + 2/p) - (2/p)(1 - (p/2)^2)^{1/2}. \tag{17}$$

This curve is plotted in Fig. 4a. This may be compared to the curve in the GRS given by (14) shown in Fig. 4b. Since both diagrams consist of a single (open) infinite line, they are topologically equivalent. Moreover, the number of turning points in pressure (local maxima) are preserved. This must be so since turning points in pressure correspond to the limit of stable equilibria, as discussed below. For bubbles and droplets, this stability limit is the basis of the “maximum bubble pressure” method of measuring interfacial tension [33, 38].

The relationship between the two diagrams (Fig. 4) can be derived analytically. Since the solution is a circular arc in the $rz$ plane, symmetrical to the $z$ axis, $z(0)$ can be expressed, by trigonometry, as

$$z(0) = \frac{\cos\alpha(0) - 1}{\sin\alpha(0)}. \tag{18}$$

Substituting (18) and (14) into (17) yields an identity.

After these preliminary remarks we proceed by describing the implementation of the PSA. The GRS, like the phase space, has the topology of a cylinder, so only solutions with $\alpha(0) \in [-\pi, +\pi]$ need be considered. We pick an arbitrary interval $p \in [p_1, p_2]$, mesh sizes $\Delta\alpha(0)$, $\Delta p$, and a value $k_{\max}$ and subdivide the given rectangle into rectangular triangles (2D-simplices) the orthogonal sides of which are equal to the corresponding meshsize. At each mesh point the function values $f_k = r_k|_{z=L} - 1$, $k \le k_{\max}$ are computed

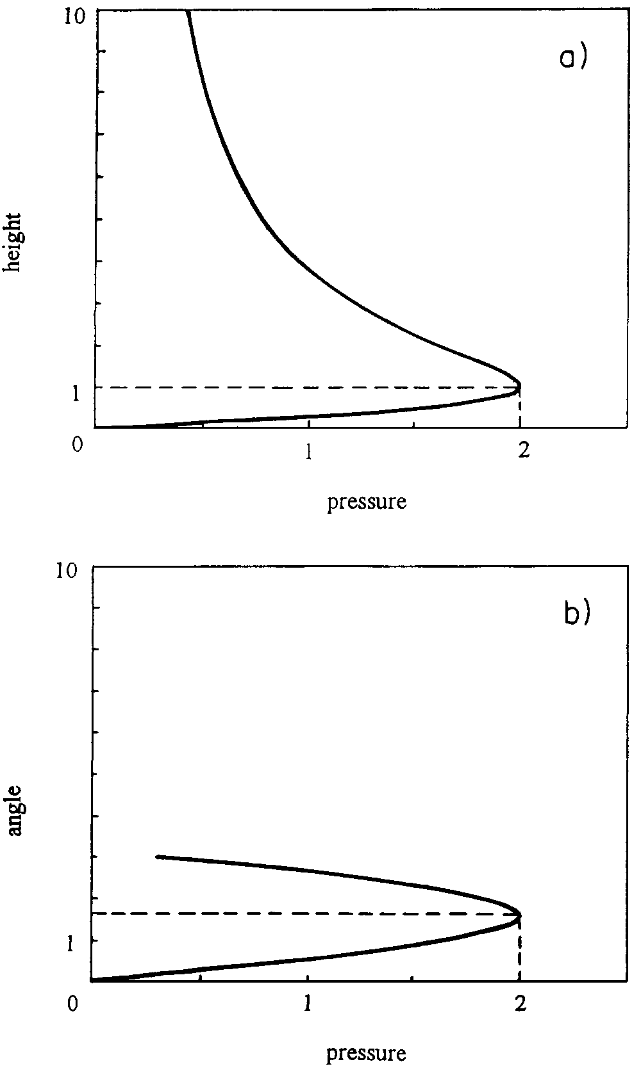

**FIG. 4.** Bifurcation curves for different GRSs show “height” $z(0)$ or “angle” $\pi - \alpha(0)$ against “pressure” $p$ for the spherical droplet (or bubble). Curve (a) plots Eq. (14) and (b) Eq. (17). In a) and b) states between the origin and turning point are stable while those beyond the turning point are unstable.

(the index $k$ refers to solution level) and the functions $f_k$ are linearly interpolated inside the simplices. If the interpolated triangle intersects the GRS inside the investigated simplex, a linearized piece of the solution branch has been obtained. The operations of the different simplices (including the evaluation of the function and the linear algebra) can be performed *simultaneously* on different processors. Thus, pieces of the bifurcation diagram emerge simultaneously, just as in photographic processing. The resulting bifurcation diagram is only approximate; however, the error at each approximate solution point can be measured exactly by substituting into the function $f_k$. The solution points are stored as a 4-vector; the two global coordinates followed by the value of $k$ and the value of the error.

We conclude this subsection by pointing out an interesting and useful feature of the GRS. The ODE (4) possesses a 3-dimensional phase space. However, the GRS is identical with that of (6). In a similar way, liquid bridges connecting disks of different diameters, that is,

**TABLE II**
**Summary for Phase Spaces and GRS**

| ODE | Phase space | BC | GRS |
|---|---|---|---|
| (4) | $[\alpha, r, z]$ | (11), (13) | $[\alpha(0), p]$ |
| (4) | $[\alpha, r, z]$ | (19), (13) | $[\alpha(0), p]$ |
| (4) | $[\alpha, r, z]$ | (15), (13) | $[\alpha(0), p]$ |
| (6) | $[\alpha, r]$ | (11) | $[\alpha(0), p]$ |
| (6) | $[\alpha, r]$ | (19) | $[\alpha(0), p]$ |
| (6) | $[\alpha, r]$ | (15) | $[\alpha(0), p]$ |

with boundary conditions

$$r(0) = 1; \qquad r|_{z=L} = r_0, \tag{19}$$

would have the same GRS. As summarized in Table II, the GRS is identical for a variety of equations and boundary conditions. This permits one not only to compute, but also to store and visualize the bifurcation diagrams in the same setting. Perhaps most importantly, it provides a connection between the various BVPs and a means for a physical understanding to be passed from one context to another.

## 3. PHYSICAL INTERPRETATION OF THE RESULTS

### 3.1. *The "Mother" Diagram: Rings and a Double Helix*

Figure 5 shows the computational results in the domain $\alpha(0) \in [-\pi, \pi]$; $p \in [-0.5, 3.5]$ for the BVP (6, 11) and (6, 15), with $L = 1$. (The latter one, corresponding to spherical solutions, is analytically given by (14).) As indicated in Table II, both BVPs belong to the same GRS (although the function to be evaluated is different). Physical shapes corresponding to numbered points are plotted on the bottom. Observe configuration No. 15 close to a *bifurcation* and No. 14 close to a *crossing*. Observe that special configurations Nos. 4 and 9 solve both BVPs.

The double-helical topology of the bifurcation diagram is also apparent from Fig. 5 if we let the $\alpha(0) = \pm\pi$ edges coincide to form a cylinder. The double helix, marked with configurations 1, 3–9, 17, 15, 16, corresponds to symmetrical shapes, as observed already by [24]. Apparently a new observation is related to asymmetric shapes, which appear on *closed*, *periodic* branches or rings. Such a branch is marked by the configurations 13, 14, 15, 10. We emphasize that such global observations on the topology of the bifurcation diagram are made evident by the PSA computations, which provide a global picture in an automated way.

Figure 6 shows the axonometric view of the 3D (*xyz*) embedding of the bifurcation diagram. The space was constructed by letting $x \equiv \cos\alpha(0)$; $y \equiv \sin\alpha(0)$; $z \equiv p$. Vertical lines correspond to $\alpha(0) = \text{constant}$, horizontal circles to $p = \text{constant}$. Only the $\alpha(0) \in [0, \pi]$ portion of the separatrix (14) is displayed. Observe that the separatrix corresponds to a *planar cut* of the cylinder, resulting in an ellipse. Figure 6a illustrates the double-helical structure of the symmetrical branch; a few physical configurations are identified. Figure 6b illustrates two periodic branches, carrying asymmetrical shapes.

The physical shapes displayed in Figs. 5 and 6 have not been stored when the diagram was computed. Rather, they were re-created by identifying the relevant points of the GRS on the bifurcation curve and using global coordinates to integrate the ODE forward. This

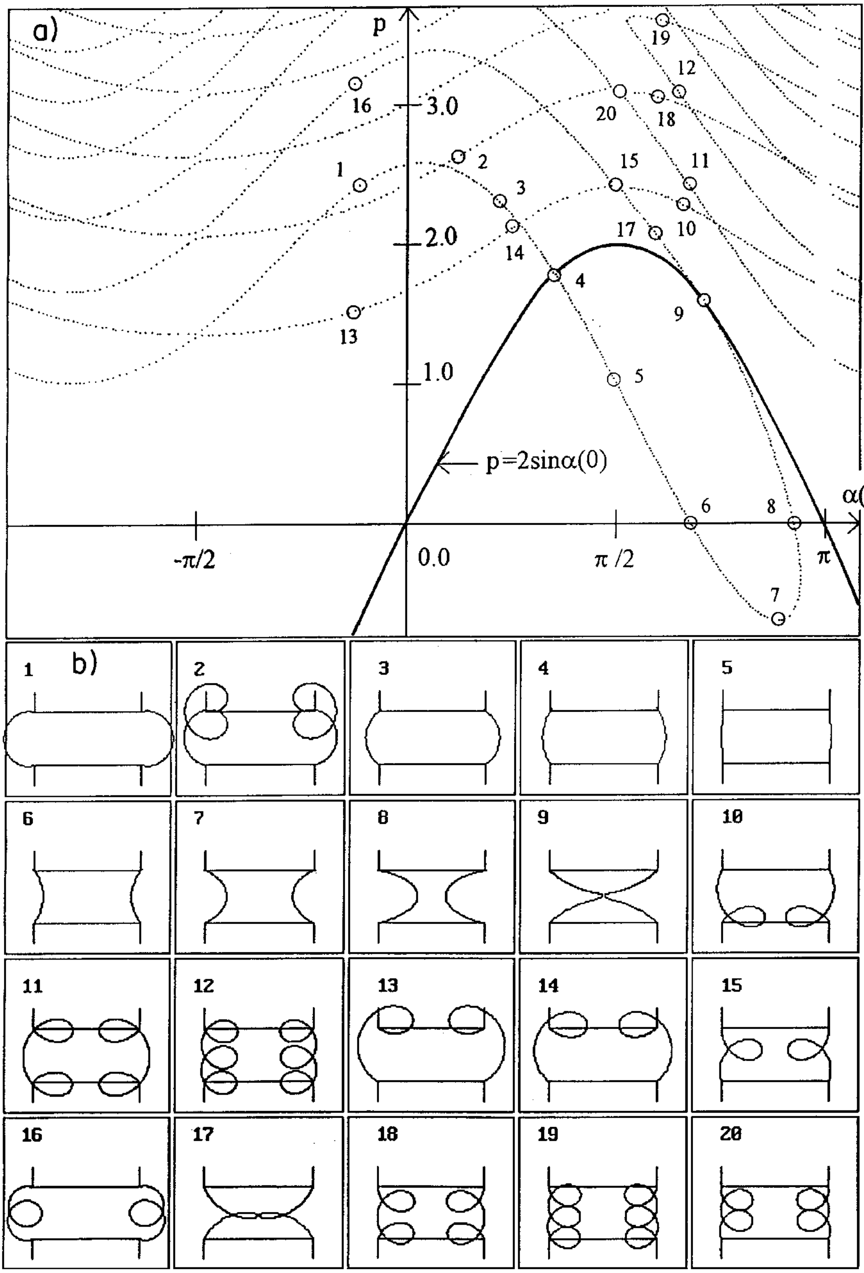

**FIG. 5.** Global bifurcation diagram for the $L = 1$ weightless bridge ($B = 0$). (a) Plot in the $[\alpha(0),\ p]$ GRS supplemented by separatrix (14) and by numbered special points. (b) Physical configurations correspond to numbered points.

idea makes it easy to visualize PSA computation results interactively. One visualization software application is described in [12].

We speak above of "physical" shapes but many of the 20 shapes shown in Fig. 5 are not realizable in the laboratory. Equilibrium shapes may not be physically realizable because they violate a physical constraint (self-intersecting and/or apparatus-intersecting, e.g., No. 2,

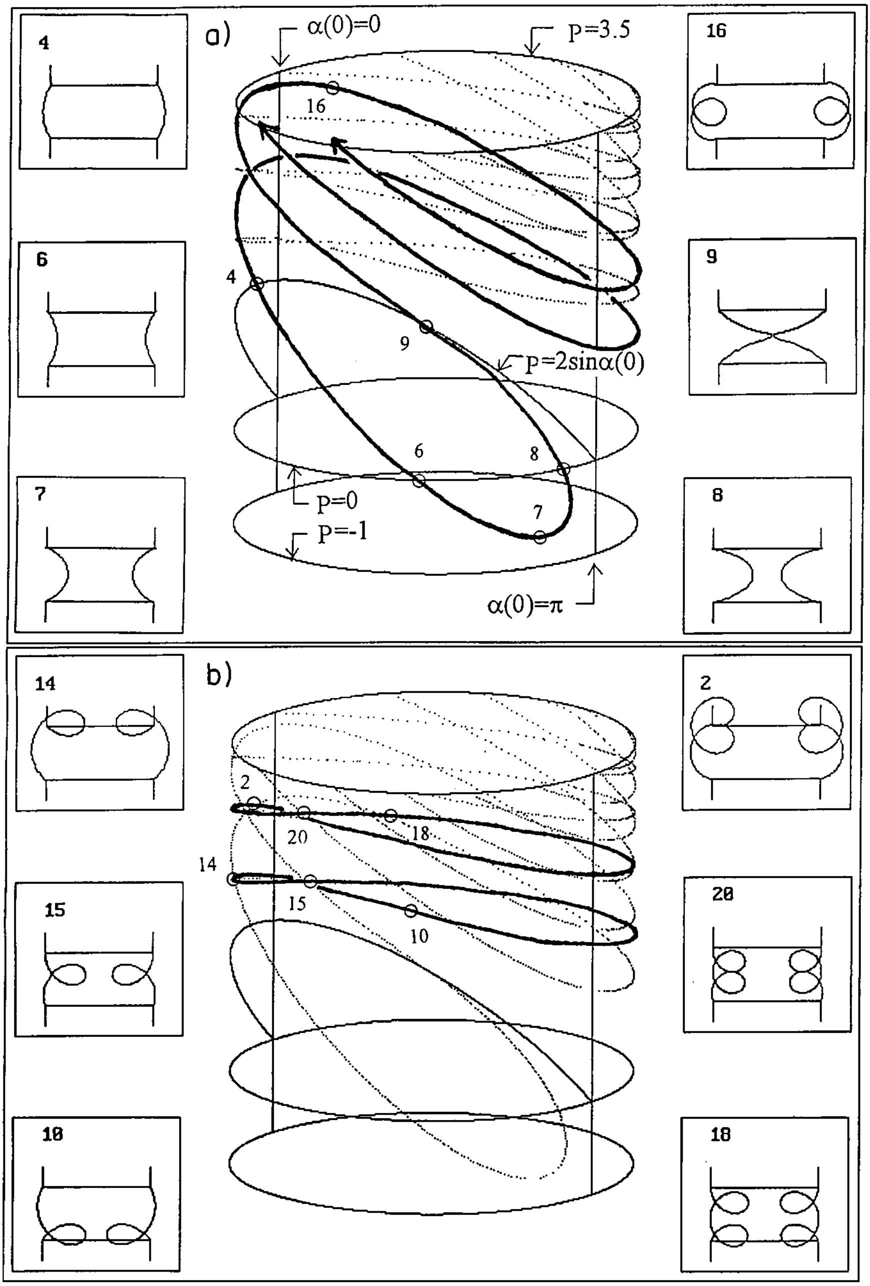

**FIG. 6.** Special structure of branches displayed on the cylindrical version of the GRS. (a) Double-helical structure of single branch carries all symmetrical shapes. (b) Two lowest periodic branches (rings) carry asymmetrical shapes.

11–20) or because they are unstable. Note that the asymmetric states in the rings are self-intersecting.

Whether or not a shape is unstable depends on the class of disturbances to which the configuration is subjected. For figures of equilibrium, stability to constant-pressure, constant-volume, axisymmetric, or general perturbations (axisymmetric and non-axisymmetric) is important. For states with single-valued $r(z)$ profiles ($0 \leq \alpha(0) < \pi$ along the symmetric branch), it is known that axisymmetric perturbations are more dangerous than non-axisymmetric ones [16, 32]. Moreover, it is known that the bifurcation to non-axisymmetric shapes occurs at $\alpha(0) = 0$ [27]. Therefore, shape 1 in Fig. 5, for example, will be unstable to a 3D shape perturbation. We therefore restrict our attention to the $0 \leq \alpha(0) < \pi$ segments of the symmetric branch where, to determine instability, it is sufficient to consider axisymmetric disturbances only.

For purposes here, it is sufficient to discuss instability with regard to constant-pressure perturbations. In this case, theory dictates that the stability/instability can be read off a bifurcation diagram where pressure is the control parameter [25]. In particular, the number of modes of instability is related to the number of "turning points" in the bifurcation curve. For example, with regard to Fig. 5, shapes 6 and 8 both correspond to catenoids. One is stable and the other unstable. This can be readily deduced by observing that (i) shape 4, a piece of a sphere, is known to be stable and (ii) there are no turning points between shape 4 and 6 so that, according to the theory, catenoid 6 must also be stable. It then follows that catenoid 8, separated from 6 by one turning point, is unstable with a single mode of instability. Such stability/instability results can also be obtained directly, but more tediously, by considering the second variation of the energy functional, the solution of whose Euler–Lagrange equations are given in Fig. 5 [31].

In the engineering literature, liquid bridge length $L$ and volume $V$ are typically considered as control parameters. The cylindrical state 5 (Fig. 5) exists for all lengths and goes unstable to constant-volume disturbances at $L = 2\pi$, the so-called Plateau–Rayleigh limit. For this reason, studies often include a range of $L$. Using continuation methods, Lowry [24] has reported a double helix consistent with Fig. 5 and has documented its evolution with $L$ over a range $0 < L < 28$. He finds that succeeding pieces of the helix disconnect at specific lengths with the first disconnection occurring at $L \approx 9.10$. He argues that this is relevant to the physics of stabilization (efforts to suppress the Plateau–Rayleigh instability). It may be noted that a convenient summary of the stability limits for weightless bridges ($B = 0$) between equal diameter contacts ($r_0 = 1$) for $0 < L < 6$ is available [15].

In the next subsection we generalize the BVP in order to better understand the difference between crossings and bifurcations and also to illustrate the power of the PSA for studying multi-parameter problems.

### 3.2. *Unequal Disks: Bifurcation Diagrams as Level Sets*

As summarized in Table II, there are many different extensions of the BVP (6, 11) which can be investigated in the same GRS $[\alpha(0), p]$. We first discuss the case of unequal disks (1). Boundary conditions (11) are replaced by (19). The bifurcation *function* (1) $g(\alpha(0), p) - 1$ is replaced by $g(\alpha(0), p) - r_0$. This implies that bifurcation diagrams corresponding to different values of $r_0$ not only can be plotted in the same plane (same GRS), but also emerge as *level sets* of the same surface $g(\alpha(0), p)$. Since, as illustrated in Fig. 3, solutions can belong to different levels, we are investigating multiple, piecewise smooth surfaces simultaneously.

If two intersecting curves of the $r_0 = 1$ "mother" diagram happen to belong to the same level, then a slight variation of $r_0$ results in slicing the same smooth surface with an adjacent, parallel plane, producing an unfolding of the bifurcation point in the sense of elementary catastrophe theory [29]. However, if the intersecting curves belong to *different* surfaces then transversality is robust and a small variation of $r_0$ will not change the local picture

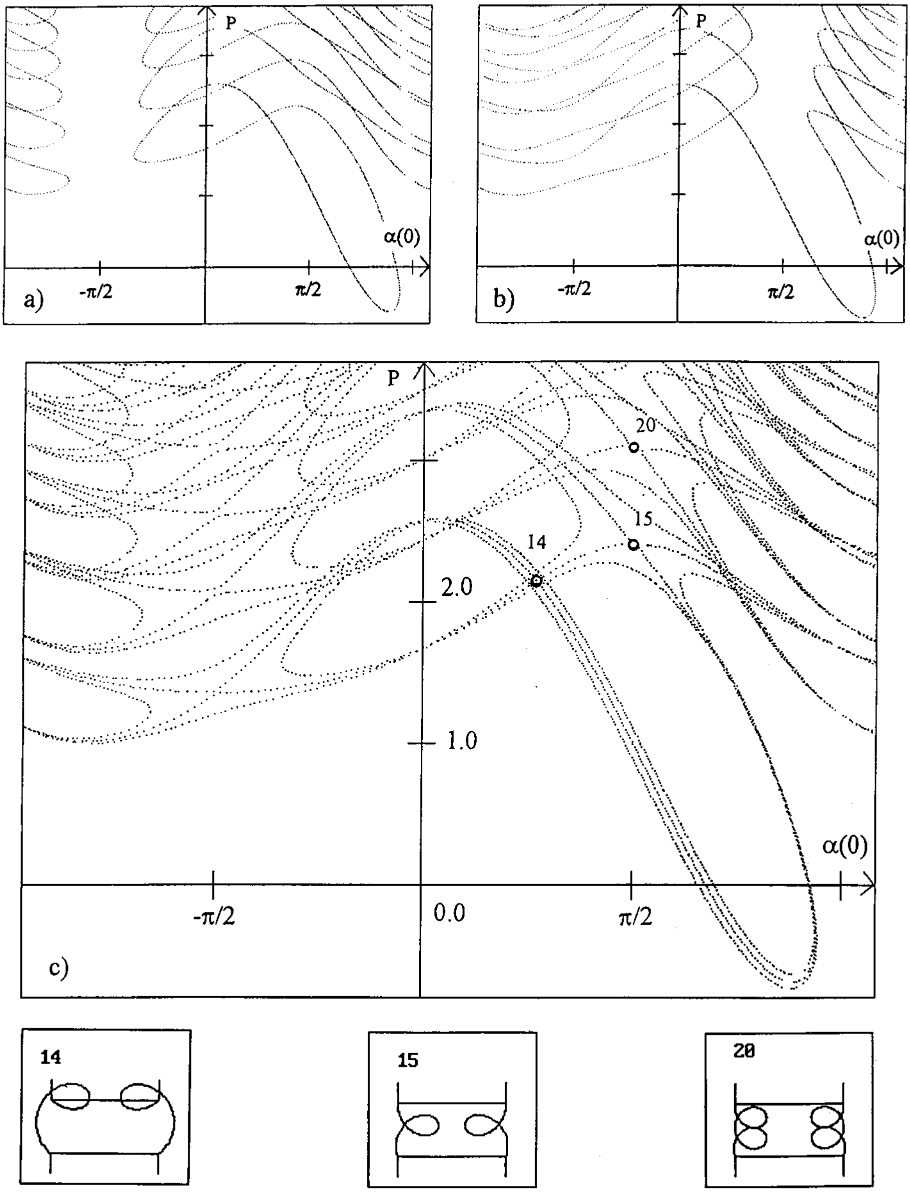

**FIG. 7.** Global bifurcation diagram ($L = 1$, $B = 0$) for unequal disks. (a) $r_0 = 0.95$; (b) $r_0 = 1.05$; (c) diagram with $r_0 = 0.95$; 1.00; 1.05 plotted simultaneously. Observe the unfolding of bifurcation points (15, 20) and the persistence of crossings (14).

qualitatively. The above features are nicely illustrated in Fig. 7, showing the $r_0 = 0.95$; 1.00; 1.05 diagrams. Observe that the bifurcation points correspond to the intersection of the double helix of symmetric solutions with the periodic asymmetric branches. These bifurcation points all lie on two vertical lines, $\alpha(0) = \pm\pi/2$. One also observes the crossings as transversally intersecting curves. These are preserved under perturbation.

This observation leads to an immediate result, a new result, as far as we are aware. The range of pressure stability, $[0, p_{\min}]$, decreases as $r_0$ decreases. That is, $p_{\min} < 0$ increases

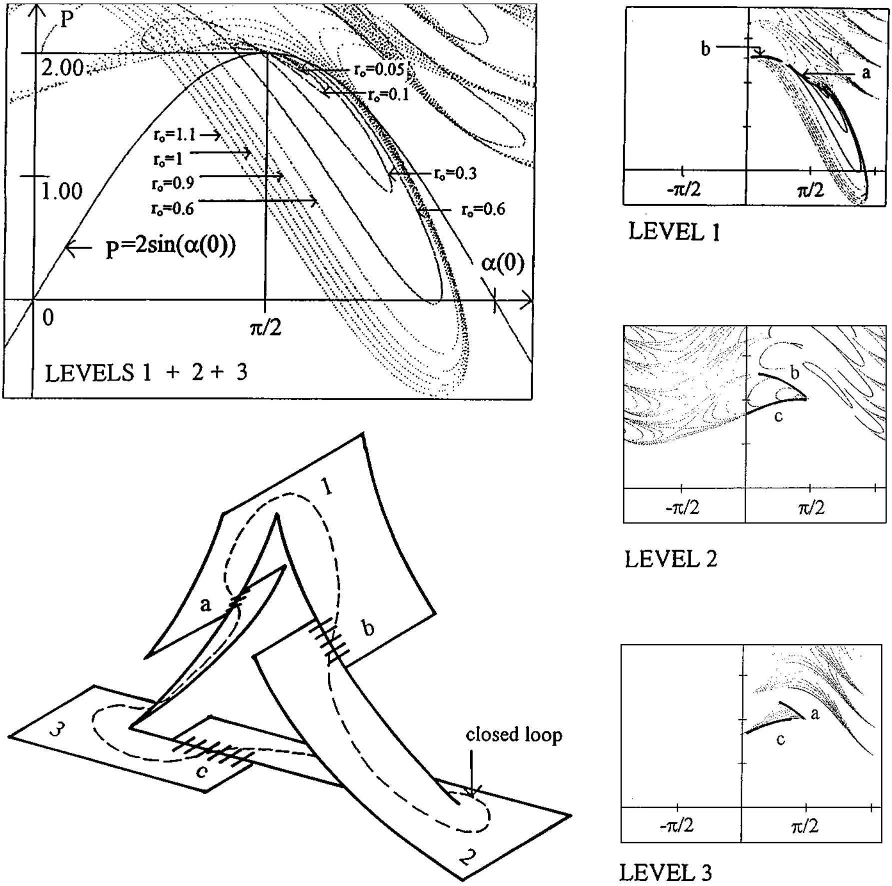

**FIG. 8.** Level 1 + Level 2 + Level 3 show BVP solutions for $0.05 \le r_0 \le 1.1$. Level 1, 2, and 3 solutions are displayed separately on right. Observe edges *a, b, c* corresponding to discontinuities (cuts). Bottom left sketch illustrates the topology of the assembly, showing a closed loop. Observe closed loop on upper bifurcation diagram shrinking onto $(\alpha(0), p) = (\pi/2, 2)$ as $r_0 \to 0$.

as $r_0$ decreases (cf. Fig. 8, level 1). This behavior is physically reasonable since the average slenderness increases for $r_0 < 1$ and decreases for $r_0 > 1$. Increasing (decreasing) average slenderness destabilizes (stabilizes). Note especially that the level set feature makes this a global result, true for all $0 \le r_0 < 1$, for example. Contrast this to what a perturbation calculation would deliver. Results for corresponding volume-stability limits for unequal supports have been obtained by a conventional approach [36].

As noted in Fig. 7a, in the case of $r_0 < 1$, the diagram consists of disconnected, isolated loops. (One of the key advantages of the PSA is that it makes possible to compute such diagrams.) If we decrease $r_0$ further, the loops shrink and at some critical value they become isolated points and then disappear. The interpretation of such an isolated point is clear for the lowest loop, as illustrated in Fig. 8.

As $r_0 \to 0$ we obtain a hemisphere as limiting solution, which is also the $\alpha(0) = \pi/2$ solution on the separatrix (14) corresponding to the single droplet. This is a degenerate BVP. It has been discussed with respect to volume-stability limits in [34]. A small perturbation of the boundary conditions will result in the disappearance of the solution. Similarly degenerate states also exist for the other rings; however, their physical interpretation is less obvious.

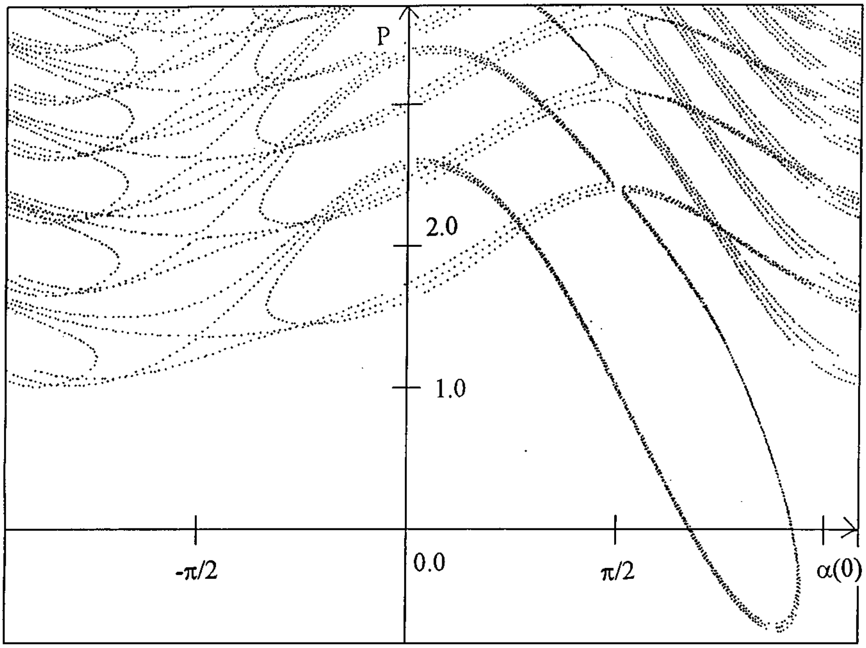

**FIG. 9.** Global bifurcation diagrams for $L = 1$ bridge under gravity; $B = -0.05$, 0.0, 0.05. Observe point marked by arrow indicating that imperfect diagrams do not represent slices of a surface represented by a function, in contrast to Figs. 7 and 8.

As Fig. 8 illustrates, the smooth bifurcation curves live on nonsmooth, noncontinuous surfaces "assembled" along discontinuities. The bottom left sketch in the figure illustrates the topology of such an assembly: the closed loop illustrated is toplogically equivalent to the $r_0 < 1$ loops observed in Fig. 7 and 8.

The PSA can be used to explore other parameter-dependent global behavior. Figure 9 illustrates the $B = -0.05$; 0; 0.05 global diagrams for the pinned–pinned bridge under gravity, associated with Eq. (4) and boundary conditions (11). We can observe *qualitatively* the same phenomenon with respect to bifurcation points as in the case of unequal disks. However, observe the point marked by the arrow. Superposed bifurcation diagrams intersect near a generic bifurcation point, indicating that different values of $B$ imply different functions $g(\alpha(0), p)$ in (1), in contrast to the case of different values of $r_0$. For equal endplates, pressure-stability limits for bridges under gravity [25] and volume-stability limits for nonzero gravity [35] have been reported, both using conventional computational approaches.

## 4. CONCLUSIONS

A novel algorithm (PSA) for obtaining families of solutions of two-point boundary value problems is described. The approach is based on integrating the underlying IVP in parallel, from a grid of initial conditions. Application of the PSA to the study of bifurcation diagrams for liquid equilibria highlights several advantages of the algorithm.

*Isolated branches.* Families of solutions that are not connected to other branches are readily captured. In the liquid bridge example, isolas on the cylinder occur with perturbations of gravity ($B \neq 0$) and of disk inequality ($r_0 \neq 1$).

*Global diagrams*. An immediate global overview of the bifurcation diagram is provided. This gives, for example, a quick recognition of the rings and the double helix structure for the weightless bridge (Fig. 6). Global information is valuable since regions that are nonphysical for one set of parameter values can become physical for another, that is, under problem deformation.

*Diagram deformation*. Snapshots of how a bifurcation diagram "deforms" as the problem deforms are readily accessible. For example, disk inequality breaks the double helix on the cylindrical phase space in one of two ways: into a simply connected or into a non-simply connected loop, depending on whether $r_0 < 1$ or $r_0 > 1$ (Figs. 7a and 7b).

Deformation is helpful in understanding families of problems. By varying end disk diameter, the liquid droplet is recovered as a limiting case of the liquid bridge. Varying end disk diameter deforms bifurcation diagrams as a sequence of "level sets" of an underlying function. Powerful results are available in such cases. Complications due to the fact that bifurcation curves are patched together from several functions can be resolved (e.g., Fig. 8). Some new stability results are obtained using the approach.

We have shown that one BVP can have more than one GRS. This observation raises the question (an open question) as to whether there is a "preferred" GRS for the understanding of a particular BVP deformation.

The main limitation of the PSA is due to computational demand. The cost of tiling the GRS into simplices grows exponentially with the dimension of the problem. (Diagrams for the 2D liquid bridge problem can be computed on a desktop.) Currently, the PSA is restricted to low- ($n < 10$) dimensional BVPs. For $n > 2$ problems, computational resolution of the intersections of hypersurfaces can yield spurious solutions which have to be filtered separately [14].

We envision the PSA as a *complement* to path-continuation techniques. For low-dimensional problems (model problems), it gives a relatively complete picture. For higher-dimensional problems, its role is to facilitate the global understanding of diagrams at an initial stage. For example, it could be used to scan the parameter space at low resolution. Diagrams could be subsequently refined by using path continuation.

## ACKNOWLEDGMENTS

G.D. and I.Sz. gratefully acknowledge financial support from OTKA under Grant T031744 and T025256 and from the U.S.–Hungarian Science and Technology Joint Fund under Project 656/96. P.H.S. thanks NASA Grant NAG3-1584 for partial support and Professor Brian Lowry for useful discussions.

The parallel computations were performed on the IBM SP2 supercomputer machine at the Cornell Theory Center (CTC). The authors thank Chris Pelkie (CTC) for help in the visualization of computational results.

The CTC receives funding from Cornell University, New York State, the National Center for Research Resources at the National Institutes of Health, the National Science Foundation, the Department of Defense Modernization Program, and members of the Corporate Partnership Program.

## REFERENCES

1. E. L. Allgower and K. Georg, *Numerical Continuation Methods: An Introduction* (Springer, Berlin, 1990).
2. F. Bashforth and J. C. Adams, *An Attempt to Test the Theories of Capillary Action* (Cambridge Univ. Press, 1883).
3. E. Blaisdell, The physical properties of fluid interfaces of large radius of curvature, *J. Math. Phys. Inst. Tech.* **19**, 186 (1940).

4. E. A. Boucher and M. J. B. Evans, Pendant drop profiles and related capillary phenomena, *Proc. R. Soc. London Ser. A* **346**, 349 (1975).
5. W. C. Carter, The forces and behavior of fluids constrained by solids, *Acta Metallurgica* **36**, 2283 (1988).
6. P. Concus and R. K. Finn, On capillary surfaces in the absence of gravity, *Acta Math.* **132**, 177 (1974).
7. S. R. Coriell, M. R. Hardy, and M. R. Cordes, Stability of liquid zones, *J. Colloid Interface Sci.* **60**, 126 (1977).
8. E. J. Doedel, H. B. Keller, and J. P. Kernévez, Numerical analysis and control of bifurcation problems: (1) Bifurcation in infinite dimensions, *Int. J. Bifurc. Chaos* **1**, 493 (1991).
9. E. J. Doedel, H. B. Keller, and J. P. Kernévez, Numerical analysis and control of bifurcation problems: (2) Bifurcation in finite dimensions, *Int. J. Bifurc. Chaos* **1**, 745 (1991).
10. G. Domokos, Global description of elastic bars, *Z. Angew. Math. Mech.* **74**(4), T289 (1993).
11. G. Domokos and Zs. Gáspár, A global, direct algorithm for path-following and active static control of bar structures, *J. Struct. Mach.* **23**(4), 549 (1995).
12. G. Domokos and R. Paffenroth, A case study for visualization for boundary value problems in *IEEE Computer Society '94 Conference Proc.* (IEEE Computer Society Press, Los Alamitos, CA, 1995), p. 345.
13. R. Finn, *Equilibrium Capillary Surfaces* (Springer-Verlag, New York, 1986).
14. Zs. Gáspár, G. Domokos, and I. Szeberényi, A parallel algorithm for the global computation of elastic bar structures, *J. Comp. Ass. Mech. Eng. Sci.* **4**(1), 55 (1997).
15. R. D. Gillette and D. C. Dyson, Stability of fluid interfaces of revolution between equal solid circular plates, *Chem. Eng. J.* **2**, 44 (1971).
16. R. D. Gillette and D. C. Dyson, Stability of axisymmetric liquid–fluid interfaces towards general disturbances, *Chem. Eng. J.* **3**, 196 (1972).
17. J. Guckenheimer, M. R. Myers, F. J. Wicklin, and P. A. Worfolk, *dstool: A Dynamical Systems Toolkit with Interactive Graphical Interface*, Center for Applied Mathematics, Cornell University, 1991.
18. P. Holmes, Oral communication to the authors.
19. P. Holmes, G. Domokos, J. Schmitt, and I. Szeberényi, Constrained Euler buckling: An interplay of computation and analysis, *Comput. Methods Appl. Mech. Eng.* **170**, 175 (1998).
20. W. Howe, Ph.D. dissertation (Friedrich–Wilhelms–Universität zu Berlin, 1887).
21. E. Kreyszig, *Differential Geometry* (Univ. of Toronto Press, Toronto, 1959).
22. D. Langbein, Stability of liquid bridges between parallel plates, *Microgravity Sci. Technol.* **1**, 2 (1992).
23. R. S. LaPlace, Traité de Méchanique Céleste (Coureier, Paris, 1806).
24. B. J. Lowry, The double-helical branch structure of fixed contact line liquid bridge equilibria, *Phys. Fluids*, in press (2000).
25. B. J. Lowry and P. H. Steen, Capillary surfaces: Stability from families of equilibria with application to the liquid bridge, *Proc. R. Soc. London Ser. A* **449**, 411 (1995).
26. J. Meseguer, Stability of slender, axisymmetric liquid bridges between unequal disks, *J. Crystal Growth* **67**, 141 (1984).
27. A. D. Myshkish et al., *Low-Gravity Fluid Mechanics* (Springer, New York, 1987).
28. J. Plateau, *Statique Experiméntale et Théorique des Liquids soumis aux seules force Moléculaires, Tome 1* (Grande et Leipzig, Paris, 1873).
29. T. Poston and I. Stewart, *Catastrophe Theory and Its Applications* (Pitman, London, 1978).
30. E. Riks, An incremental approach to the solution of snapping and buckling, *Int. J. Solids Struct.* **15**, 529 (1979).
31. A. W. Reinhold and A. W. Rücker, On the thickness and surface tension of liquid films, *Philos. Trans. R. Soc. London* **177**, 627 (1886).
32. M. J. Russo and P. H. Steen, Instability of rotund capillary bridges to general disturbances: Experiment and theory, *J. Colloid Interface Sci.* **113**, 154 (1986).
33. E. Schrödinger, Notiz über den Kapillardruck in Gasblasen, *Ann. Phys. (Lelpztg)* **46**, 413 (1915).
34. L. A. Slobozhanin and J. I. Alexander, Combined effect of disk inequality and axial gravity on axisymmetric liquid bridge stability, *Phys. Fluids* **10**(10), 2473 (1998).

35. L. A. Slobozhanin and J. M. Perales, Stability of liquid bridges between equal disks in an axial gravity field, *Phys. Fluids A* **5**(6), 1305 (1993).
36. L. A. Slobozhanin, M. Gomez, and J. M. Perales, Stability of liquid bridges between unequal disks under zero-gravity conditions, *Microgravity Sci. Technol.* **8**(1), 23 (1995).
37. T. I. Vogel, Stability of a liquid drop trapped between two parallel planes. II. General contact angles, *SIAM J. Appl. Math.* **49**(2), 1009 (1989).
38. A. Weissberger and W. Rossiter, Eds., *Physical Methods of Chemistry, V* (Wiley Interscience, New York, 1977), Chap. IX.
39. H. C. Wente, The stability of the axially symmetric pendent drop, *Pac. J. Math.* **88**(2), (1980) 421–469.
40. T. Young, An essay on the cohesion of fluids, *Philos. Trans. R. Soc. London* **95**, 65 (1805).